Supporting Information for Research Article

"Fault Friction, Plate Rheology, and Mantle Torques from a Global Dynamic Model of Neotectonics"

Peter Bird, Jon Bryan May, and Michele M. C. Carafa

in *Journal of Geophysical Research: Solid Earth*

CONTENTS:

*Improvements to Modeling Software

*Updated Scoring Datasets

*Updated Lithospheric Structure

* Figures S1 through S16

N.B. See References Cited in main paper for full-length citations.

IMPROVEMENTS IN MODELING SOFTWARE

After Paper I, dynamic thin-shell finite-element (F-E) code Shells v.3 was improved by *(i)* using 8-byte storage for all real numbers; *(ii)* use of the Intel Math Kernel Library to solve linear systems in parallel mode; and *(iii)* provision for lateral variations in rheologic constants, by optionally assigning an integer "Lithospheric Rheology index" (LRi) to each (continuum or fault) finite element, and then reading an additional table that specifies the set of real-number parameter values which that index represents. The source code was also updated to Fortan 90 syntax for better clarity. The result was Shells v.5.

More importantly, May et al. (2024) then incorporated Shells v.5 into a larger package, ShellSet v.1.1.0, which automates all steps that had previously required operator intervention, including: the computation of lithospheric-structure variables at each F-E node (program OrbData5), the iteration of the Shells solution needed to converge on proper basal strength torques for each slabless plate, and the scoring of each model's predictions against various geophysical and geologic datasets (program OrbScore). Furthermore, it added a top-level executive function that can vary selected model parameters (*e.g.*, effective coefficient of friction on all plate-boundary faults) automatically and systematically, using a self-refining grid search to estimate their optimal values. ShellSet is also able to run many alternative Shells simulations in parallel, given proper hardware support. This means that a two-parameter optimization experiment that previously required months of part-time operator intervention can now be run overnight.

As detailed in May et al. (2024), ShellSet is both compiled and run in a Linux environment. We utilized the Windows Subsystem for Unix (WSL2), loaded with secondary operating system Ubuntu, to make these computations on a Windows 10 Pro computer. The hardware included 2 Intel Xeon CPU E5-2643 processors (total 16 virtual processors), 64 GB of RAM, and a 500 W power supply. Maps of output (in Adobe Illustrator .AI format) were produced with our program FiniteMap (available from the archive of Bird (2025)).

After some initial experimentation, we decided to take advantage of this efficient hardware and software by attempting better convergence of both the inner and outer iterations that occur within a typical Shells solution. Parameter maxItr, the maximum number

of iterations of each global velocity solution (to accommodate nonlinear terms) was increased to 80 (versus 50 in Paper I), while parameter okToQt (which allows early termination of iteration if convergence meets this target) was increased to 5×10^{-4} (versus the previous unrealistic goal of 1×10^{-4}) to avoid wasted iterations. The outer loop, in which the entire Shells velocity solution is iterated to improve the representation of basal shear tractions on slabless plates, was run 10 times (versus 5 in Paper I).

UPDATED SCORING DATASETS

Geodetic velocity (GV) has been measured at thousands of benchmarks, where it is usually reported as the mean interseismic horizontal velocity vector. It might seem redundant to score model predictions against GV in a project where most plates have been forced by boundary conditions to move with approximately correct rotations, but it is actually quite valuable because our model plates are also deforming internally, and this internal deformation contains essential clues to intraplate stress fields and the related plate-driving torques. F-E model velocities are long-term averages (including coseismic strain changes), but they can be converted to interseismic predictions by subtracting the mean coseismic velocity, and this is readily done in the model universe where long-term slip-rates and rakes and locking depths of all modeled faults are known. This correction was previously explained in Paper I; the solutions we use for a dislocation patch in an elastic halfspace are those of Mansinha and Smylie (1967, 1971). Another issue is different velocity reference frames; to handle this, we add the uniform global Eulerian rotation-rate that minimizes the RMS misfit. Finally, when computing the global RMS size of velocity-misfit vectors, we weight each site by the area of Earth surface associated with it; this prevents an unhealthy bias toward matching geodetic velocities only in densely-monitored areas like Japan and California. In Paper I, the GV dataset used was the Global Strain Rate Map (Kreemer et al., 2003) data set describing 4,298 sites. In this project we used the Global Strain Rate Map version 2.1 dataset of Kreemer et al. (2014) which provides interseismic GPS velocities at 18,356 locations.

Seafloor spreading rate (SSR) is measured from widths of magnetic anomaly bands of known age along midocean rises. We compare this to heave-rates across normal fault elements that represent spreading rises in the F-E model. Again, it might seem redundant to score model predicted spreading rates in a project where most plates have been forced by boundary conditions to move with approximately correct rotations, but it is actually quite valuable because our model plates are also deforming internally. If we modeled oceanic lithosphere with a rheology that was too weak, then model spreading rates would depart substantially from rigid-plate predictions, and also from data. Here we used the same dataset as in Paper I: 277 rates from the NUVEL-1 collection in Table 3 of DeMets et al. (1990), which includes citations. We multiplied each of these rates by 0.9562 to correct for the adjustment in the

paleomagnetic reversal timescale that DeMets et al. (1994) made in their revised NUVEL-1A model. As in Paper I, we added 35 rates which were published more recently; most are from back-arc spreading systems not considered in the NUVEL models, but added in the PB2002 model of Bird (2003).

Fault slip rate (FSR) data is obtained from the offsets of pairs of piercing points with known age. It is directly comparable to long-term-average fault slip rates computed in our F-E models. FSR scoring was not used in Paper I because no global dataset existed. Here we use selected fault traces (Figure S2) and slip rates from the Global Active Fault Database (GAFD) of Styron and Pagani (2020). Specifically, we only use rates which are reported with upper and lower limits, because we note that most rates without uncertainties are from rigid plate models (e.g., Bird, 2003), not from geologic data. We also require the fault dip to be specified, for use in converting heave-rates to slip-rates. After these two restrictions, the number of faults potentially useful for scoring is reduced from 13,696 to 2,487. To associate a GAFD trace with a F-E fault element, we require that *(i)* their azimuths agree within ±15°; and *(ii)* the shortest distance between the two traces must be less than one-eighth of the length of the F-E model fault element. When multiple actual faults in a quasi-parallel set are associated with one fault element, their slip rates are summed. Under these selection rules, we obtained 570 aggregated fault slip rates usable for scoring. Unfortunately, they are heavily concentrated in a few areas (southeast Europe, Turkiye, Iran, New Zealand, California) and do not provide uniform global coverage.

Stress direction (SD) is the azimuth of the most-compressive horizontal principal stress direction. We compare this to the azimuth of the most-compressive horizontal principal strain-rate axis in the appropriate continuum element of our F-E model. However, unfiltered data lists from the World Stress Map Project (Reinecker et al., 2004; Heidbach et al., 2016; 2018) are not very suitable for testing our global dynamic models because their data are so strongly concentrated in Europe, North America, and a few other areas of high seismicity. To handle this, we interpolate stress directions (wherever possible) to a uniform global grid of points by the clustered-data algorithm of Bird and Li (1996). The result was a set of interpolated stress directions at 608 grid points in Paper I, increasing to 764 interpolated stress directions (Figure S3) in this project.

Seismic anisotropy (SA) is measured from seismograms showing arrivals of quasi-vertical S phases that have known initial polarization, such as SKS waves that have passed through the liquid outer core. Typically, many such arrivals are averaged at each seismic station to produce a mean azimuth of slow polarization, and a delay time between the fast and slow arrivals. In Paper I we used 992 selected station-averaged anisotropies from the compilation of Fouch and Rondenay (2006). In this project we use 1,528 selected 2°-trapezoid averages from file Becker_SKS_2-degree_20220807.dat, obtained from Thorsten Becker's archive at http://www-udc.ig.utexas.edu/external/becker/sksdata.html (last accessed 2022.10.24). The selection rules were exactly the same as in Paper I. We also retained the old scoring algorithm which looks for a match of slow directions to either the azimuth of simple-shear in the model asthenosphere (under slabless plates, where our model makes a prediction of simple-shear direction), or to the azimuth of the most-positive horizontal principal strain-rate axis in the lithosphere. Unfortunately, some SA observations may relate to fossil fabrics within the lithosphere; since our models are not able to predict these fabrics, and we have no global dataset of fabrics to apply, this kind of SA data just injects noise into our SA scoring and raises the global misfit statistic for every model. It is our belief that this increased misfit due to fossil fabrics is approximately the same for each model, so that SA misfit statistics are still useful for relative scoring of competing models.

UPDATED LITHOSPHERIC STRUCTURE

All versions of Shells v.3+ (and ShellSet) use a set of 6 numbers to describe the lithospheric structure and geotherm under each of the 16,008 nodes of the F-E grid. (Geotherm refers to temperature as a function of depth below a particular surface point.) These 6 numbers are: elevation, heat-flow, crustal thickness, mantle lithosphere thickness, density anomaly of chemical origin, and transient geothermal curvature due to cooling (or heating, if negative). The first two are obtained from surface data. The layer thicknesses are obtained from seismic-velocity models. The chemical density anomaly is computed (in the OrbData component of the ShellSet package) to enforce local isostasy; however, limits on the chemical density anomaly are imposed (± 50 kg m^{-3}), with the result that subduction trenches and plume-related hotspots are usually not isostatically-compensated within this model domain, implying dynamic support from mantle convection which then enhances the contribution of this topography to lithostatic pressure torques by placing some compensation below the lithosphere. (However, our models do not include dynamic topography in other places where its amplitude is less; instead, we compensate such topography by smaller adjustments to the density anomaly of chemical origin. Note that this approximation has exactly zero effect on computed lithostatic pressure torques unless the dynamic topography occurs along a plate boundary; see equation 7 in Paper I.) The geothermal curvature is computed to enforce a constant temperature at the base of the model lithosphere, whose depth varies laterally.

Within either layer (crust or mantle lithosphere), rock densities of compositional origin (at STP) do not vary with depth. (They may vary laterally, from node to node.) However, density always decreases with depth within either layer because of thermal expansion due to increasing temperature with depth. We neglect the effect of pressure on density as a self-consistent convenience.

For this project, we replaced the ETOPO5 elevations (NOAA, 1988) used in Paper I with higher-resolution ETOPO2 elevations (NOAA National Geophysical Data Center, 2006).

Heat-flow was approximated in Paper I by a composite model: age-dependent within oceanic lithosphere (using seafloor ages from Müller et al., 1997), and data-dependent (interpolated by kriging) in continental lithosphere. In this project we kept the composite

approach, but replaced the oceanic-heatflow-versus-age model of Stein and Stein (1992) with that in Figure 8(b) of Richards et al. (2018). In continental crust, we switched to the global heat-flow prediction model of Lucazeau (2019), specifically version HFgrid14.grd which incorporates other datasets (topography, seismic velocity, tectonic setting, gravity) as well as traditional borehole and probe measurements. Upper and lower bounds of 300 and 30 mW/m^2 were then applied to avoid computational problems in ShellSet. This new model can be seen in Figures S5 and S6.

Crustal thicknesses in Paper I came from the CRUST2 grid of Bassin et al. (2000), with resolution of 2°. In this project, we used the CRUST1.0 model of Laske et al. (2013), which has 1° resolution.

Mantle lithosphere thicknesses in Paper I were estimated in a complex way from upper-mantle S-wave travel-time anomalies. In this project, we use continental values from the LithoRef2018.xyz model of Afonso et al. (2019), which merged 6 tomographic models to determine upper-mantle velocities, with gravity and geoid constraints to estimate compositional density variations. However, we observed that this model tends to overpredict lithosphere thickness in the ocean basins; hence we obtained these from the age-dependent model in Figure 9(c) of Richards et al. (2018). Figure S7 displays our composite model as full lithosphere thickness (including the thickness of crust, discussed above).

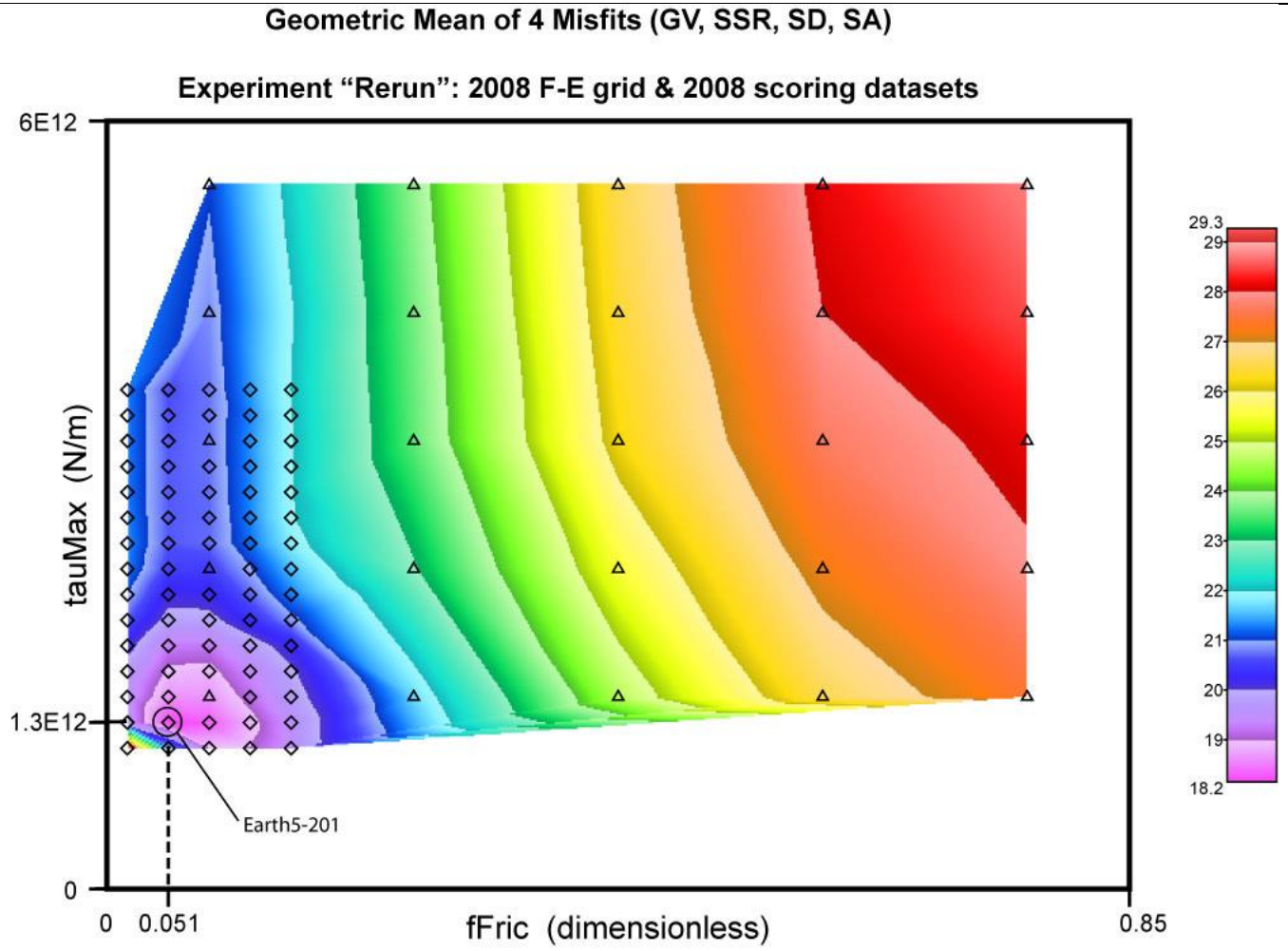

Figure S1. Results of re-running the preferred model of Paper I (Bird et al., 2008) with ShellSet. The model space is defined by two varied parameters: effective friction of fault elements fFric (horizontal axis), and down-dip integral of shear traction on subduction megathrusts tauMax (vertical axis, in N/m). The quantity contoured is the geometric mean of 4 misfits, obtained when model is compared to each of 4 scoring datasets: GV = Geodetic Velocity, SSR = Seafloor Spreading Rate, SD = Stress Direction, SA = Seismic Anisotropy. Each triangle shows a parameter combination tested by ShellSet in the first-level grid search, and each diamond shows a parameter combination tested by ShellSet after its automatic grid refinement.

127

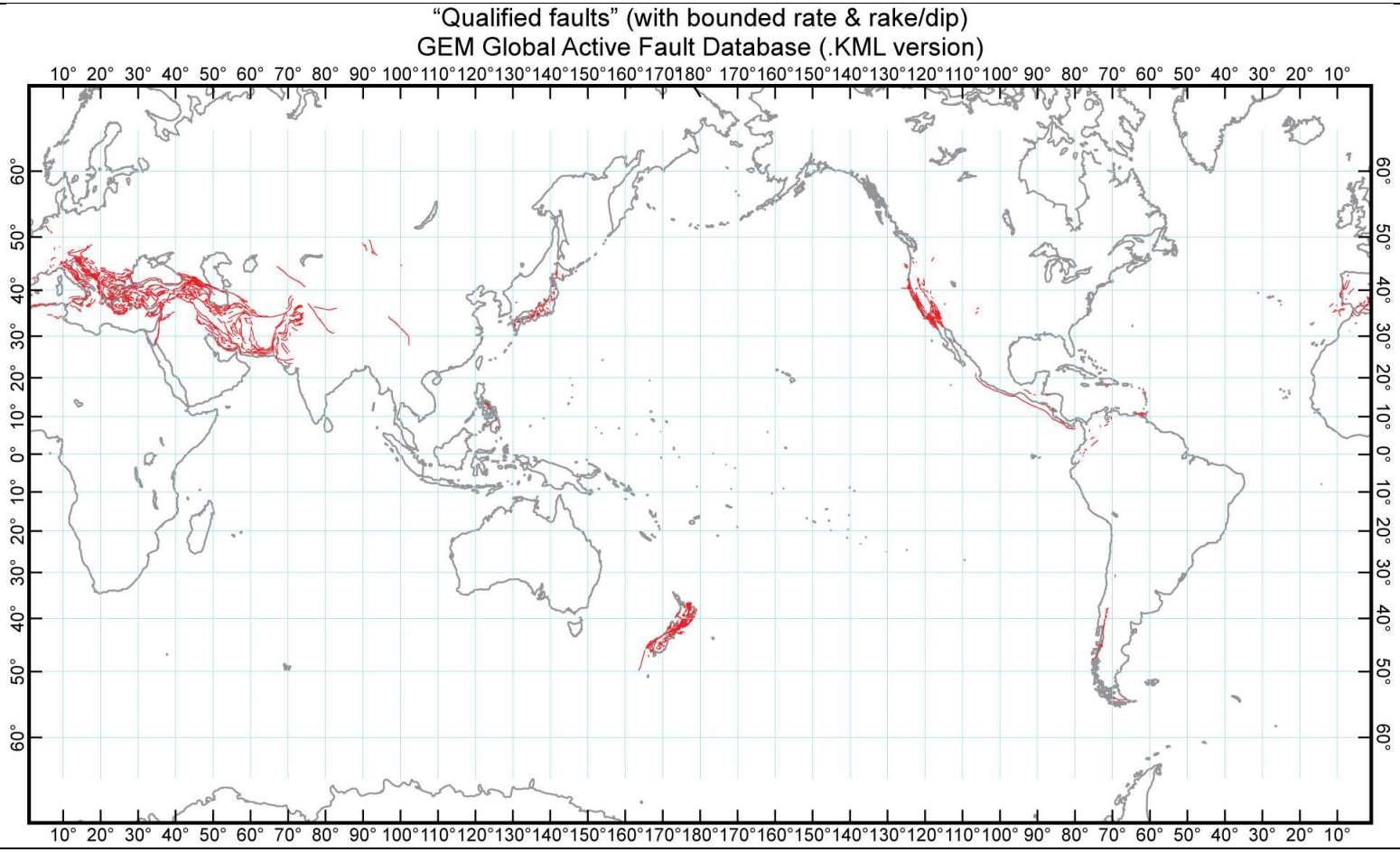

Figure S2. Traces (red lines) of active faults with known slip-rates, used for model testing as dataset FSR. All traces from the GEM Active Fault Database of Styron and Pagani (2020). We selected traces with bounded slip-rates, and with known dip and rake.

128

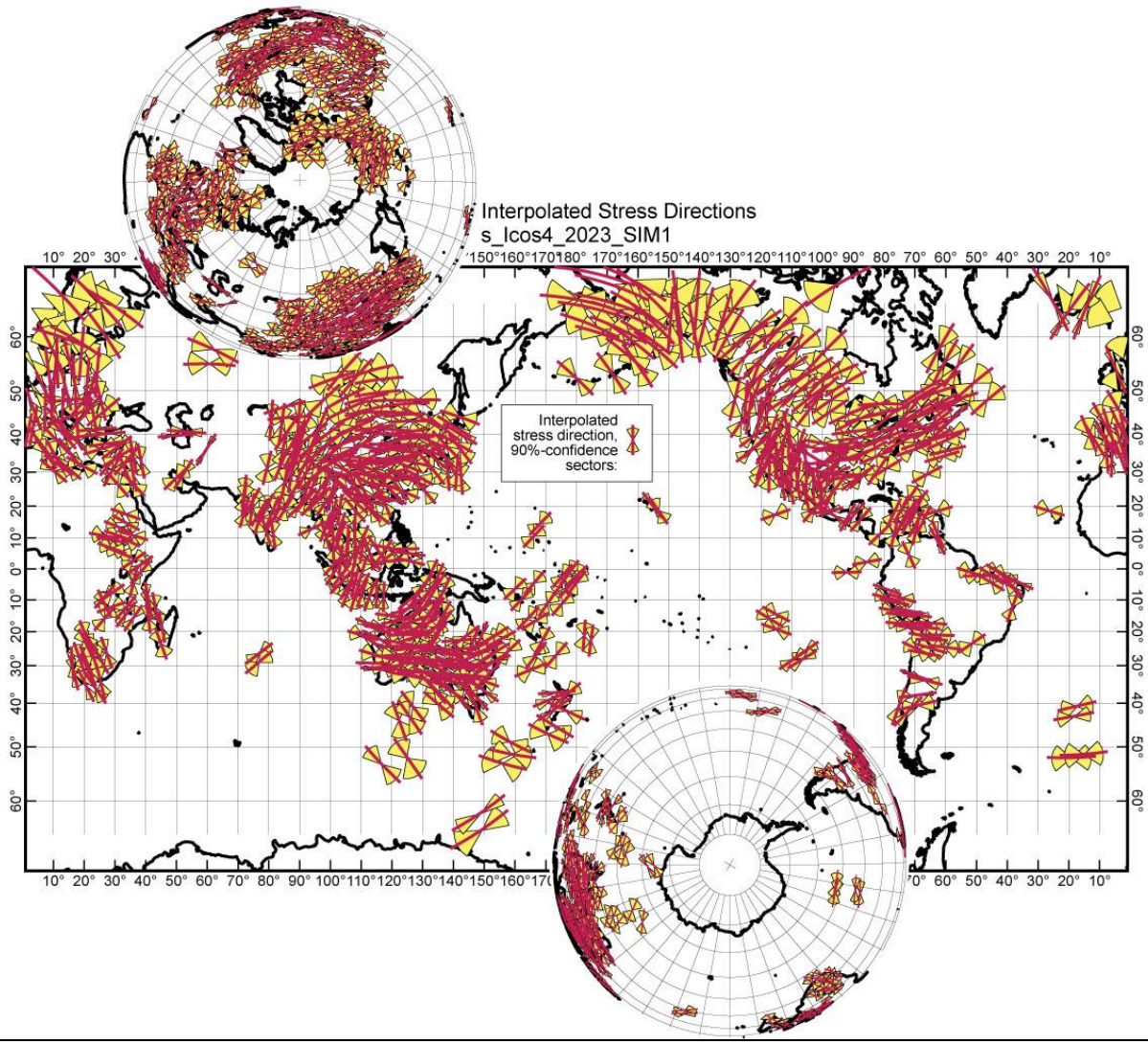

Figure S3. Interpolated azimuths of most-compressive horizontal principal stress, used for model testing as dataset SD. Source data from the World Stress Map dataset of Heidbach et al. (2016; 2018). Interpolation was by the clustered-data method of Li and Bird (1996), which provides uncertainties for each result. Yellow wedges show widths of 90%-confidence ranges in azimuth. Interpolation results with wedge widths greater than ±45° are not shown and were not used in model scoring.

129

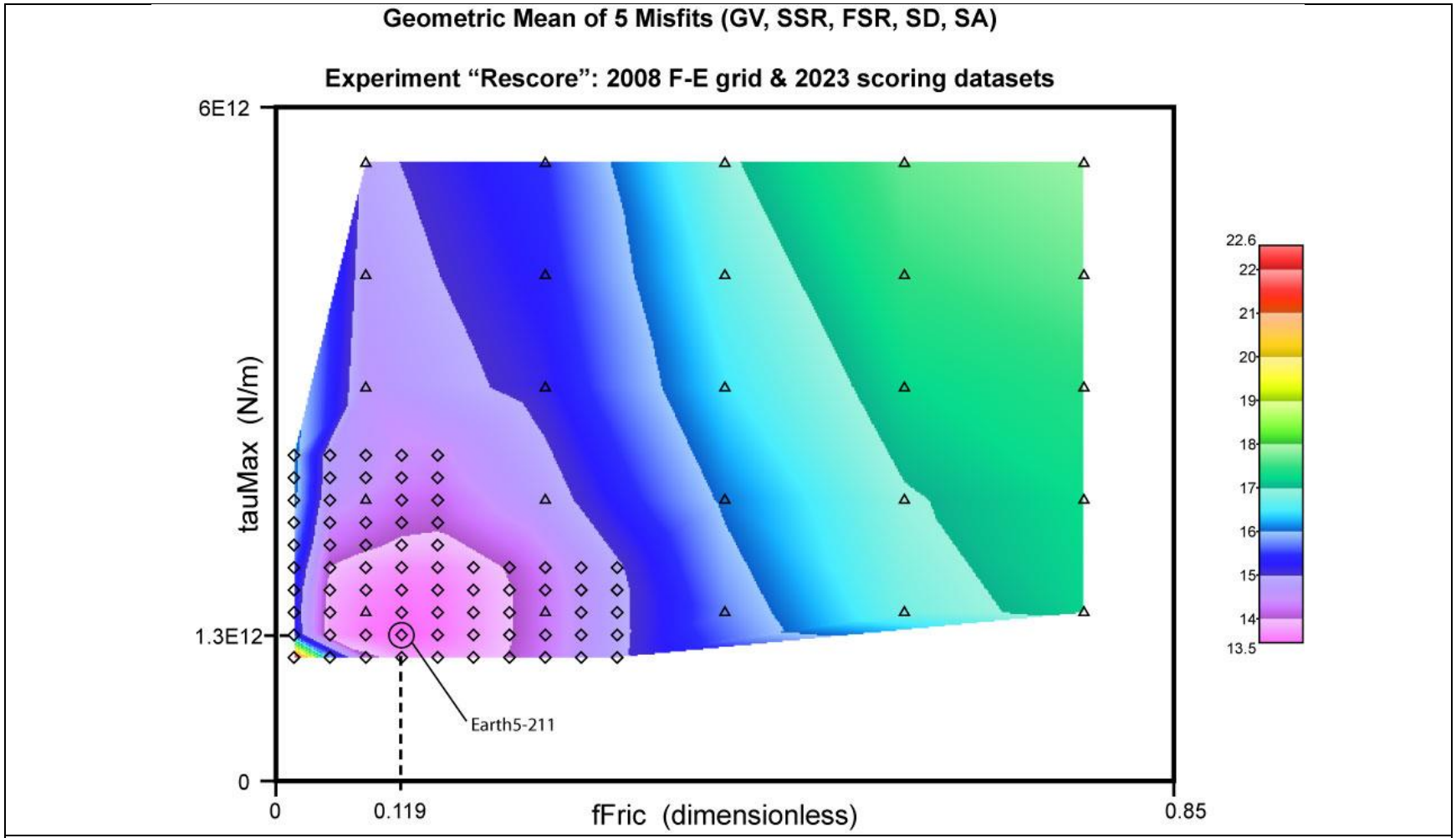

Figure S4. Results of experiment "Rescore" (see Table 1 in paper), in which the preferred model from Paper I (Bird et al., 2008) was re-run with updated scoring datasets, including the addition of new scoring dataset FSR = Fault Slip Rate. Figure conventions as in Figure S1.

130

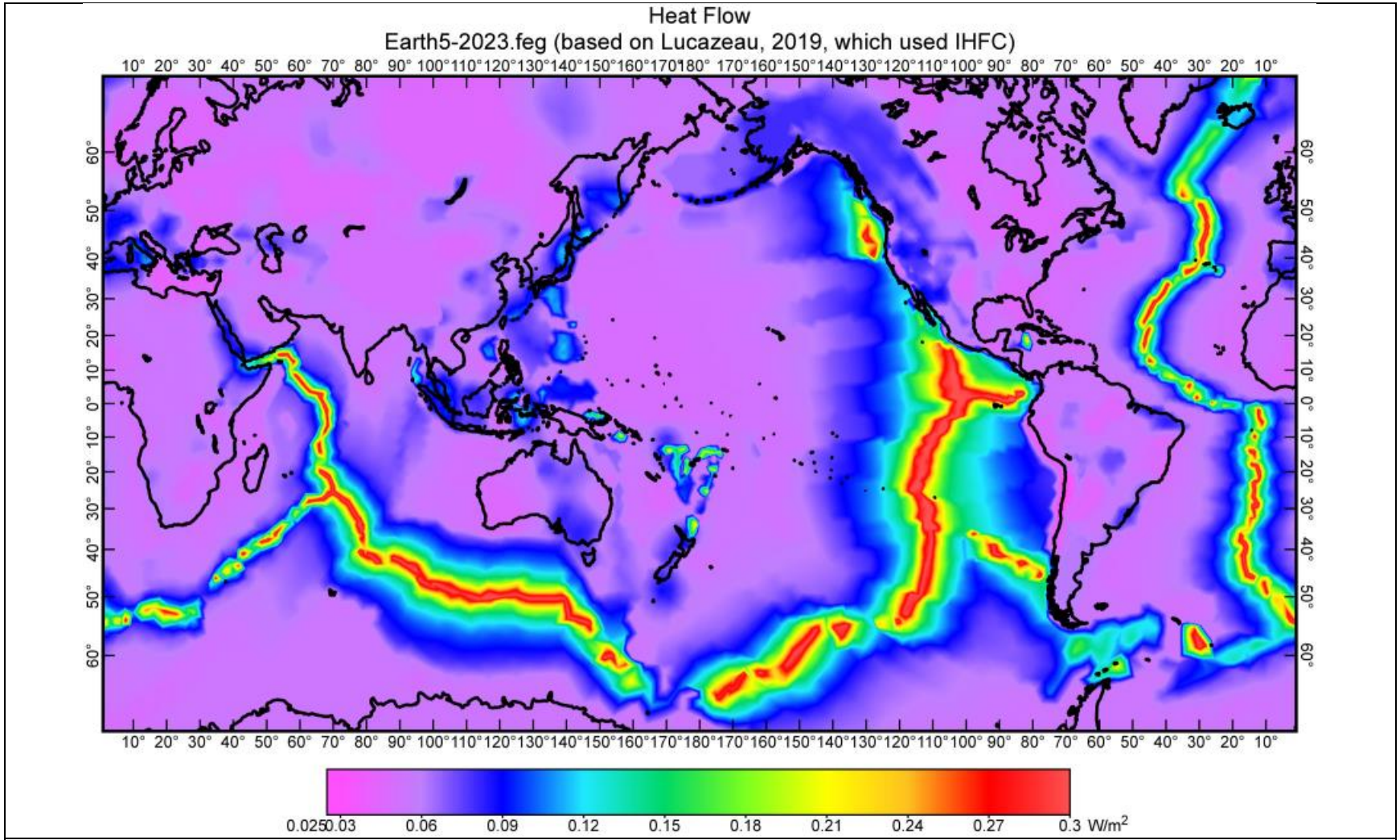

Figure S5. Updated model of global heat-flow, with continental areas based on Lucazeau (2019), and seafloor areas of known age based on Richards et al. (2018). In this figure, the color-scale is chosen to show the full range of heat-flow, making it hard to see detail in continental areas. See Figure S6 below for an expanded color scale.

131

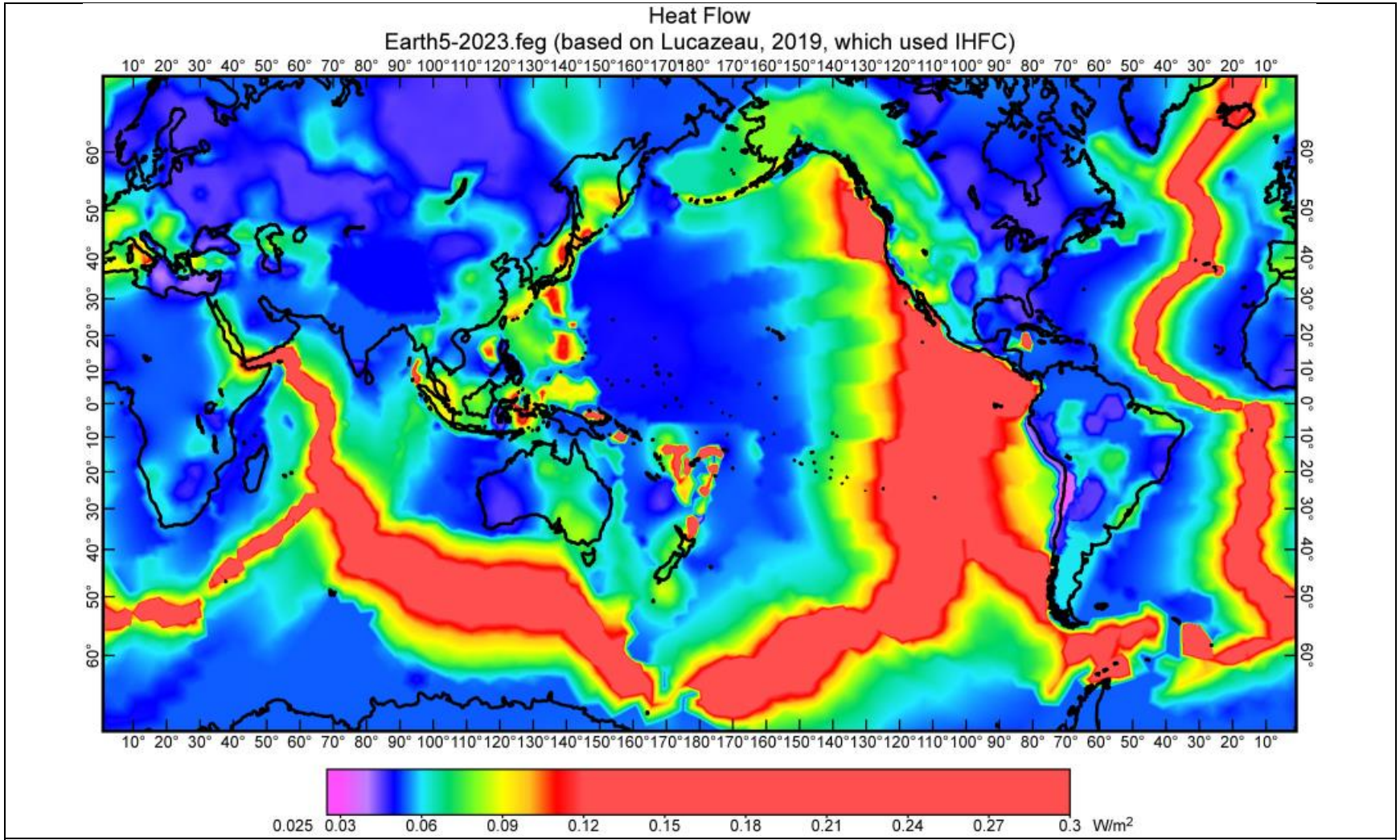

Figure S6. Updated model of global heat-flow, with continental areas based on Lucazeau (2019), and seafloor areas of known age based on Richards et al. (2018). In this figure, the color-scale is chosen to show detail in continental areas. See Figure S5 above for a full-range color scale.

132

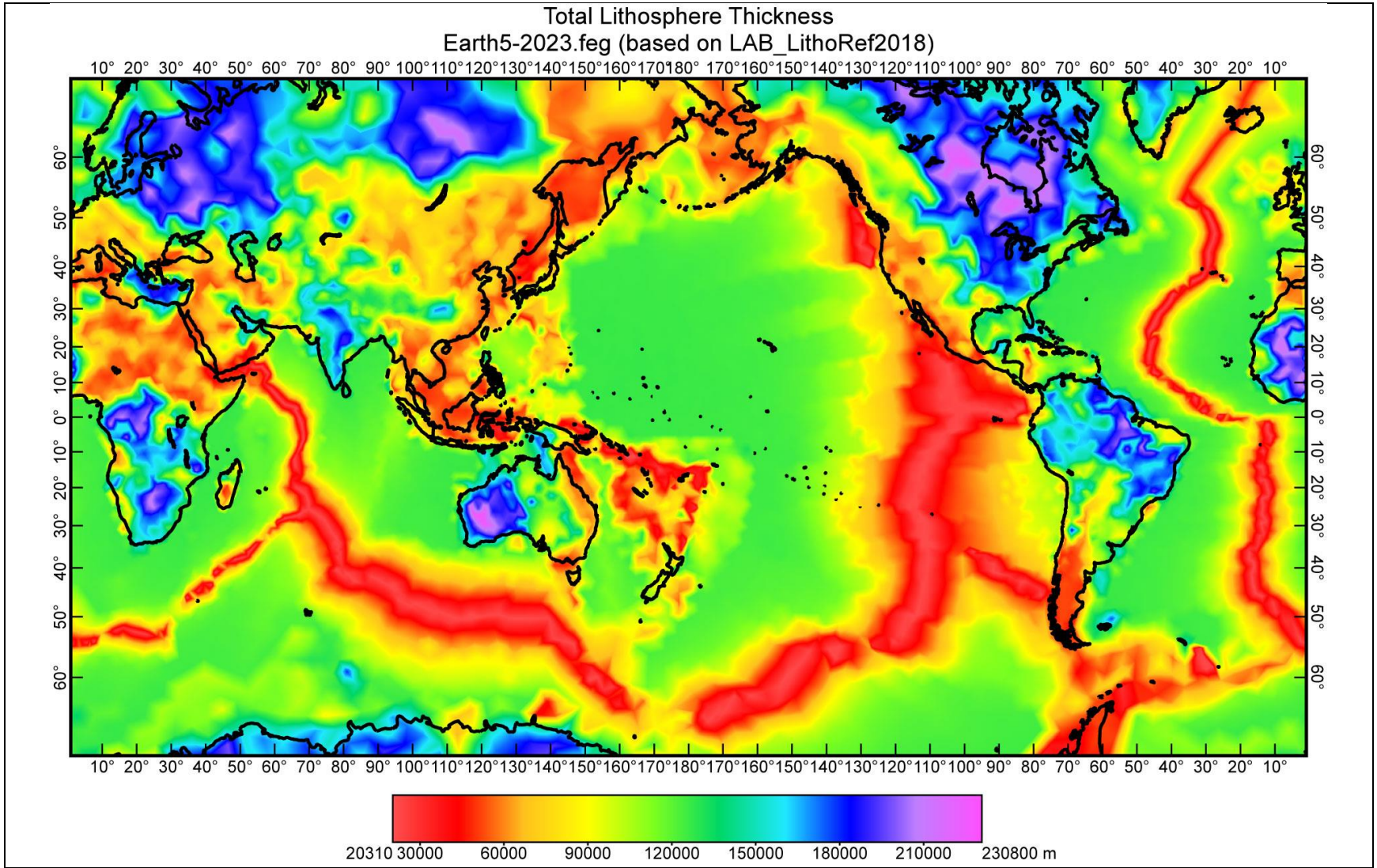

Figure S7. Updated model of full lithosphere thickness, including crustal thickness from Crust 1.0 of Laske et al. (2013) and mantle lithosphere thickness from Afonso et al. (2019) in continental areas, or from Richards et al. (2018) in seafloor areas of known age.

133

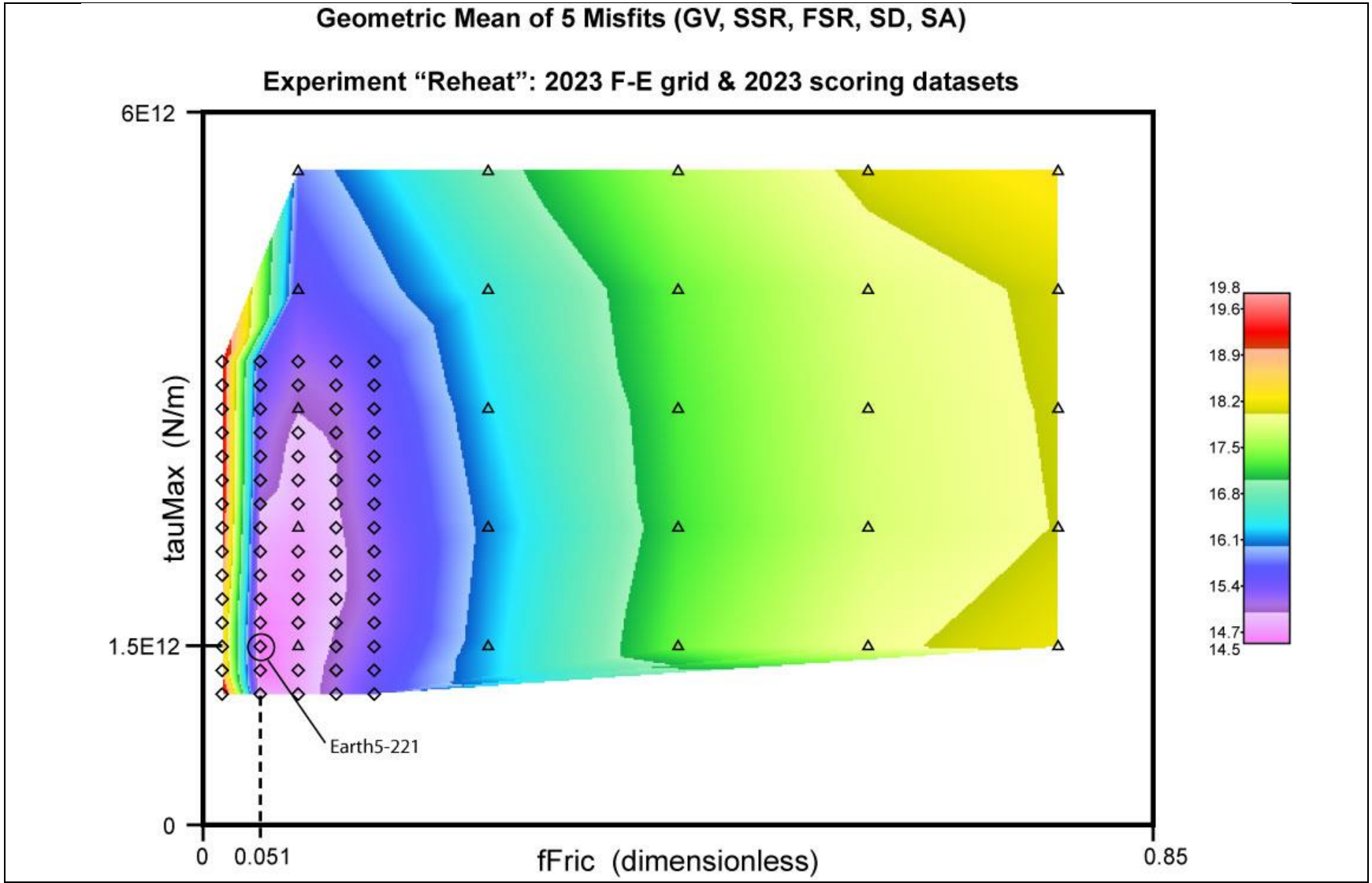

Figure S8. Results of experiment "Reheat" (see Table 1 in paper), in which we again searched for optimal plate-boundary friction parameters, but now using both the updated scoring datasets and the updated lithospheric structure (of Figures S5, S6, S7 above). See Figure S1 for figure conventions.

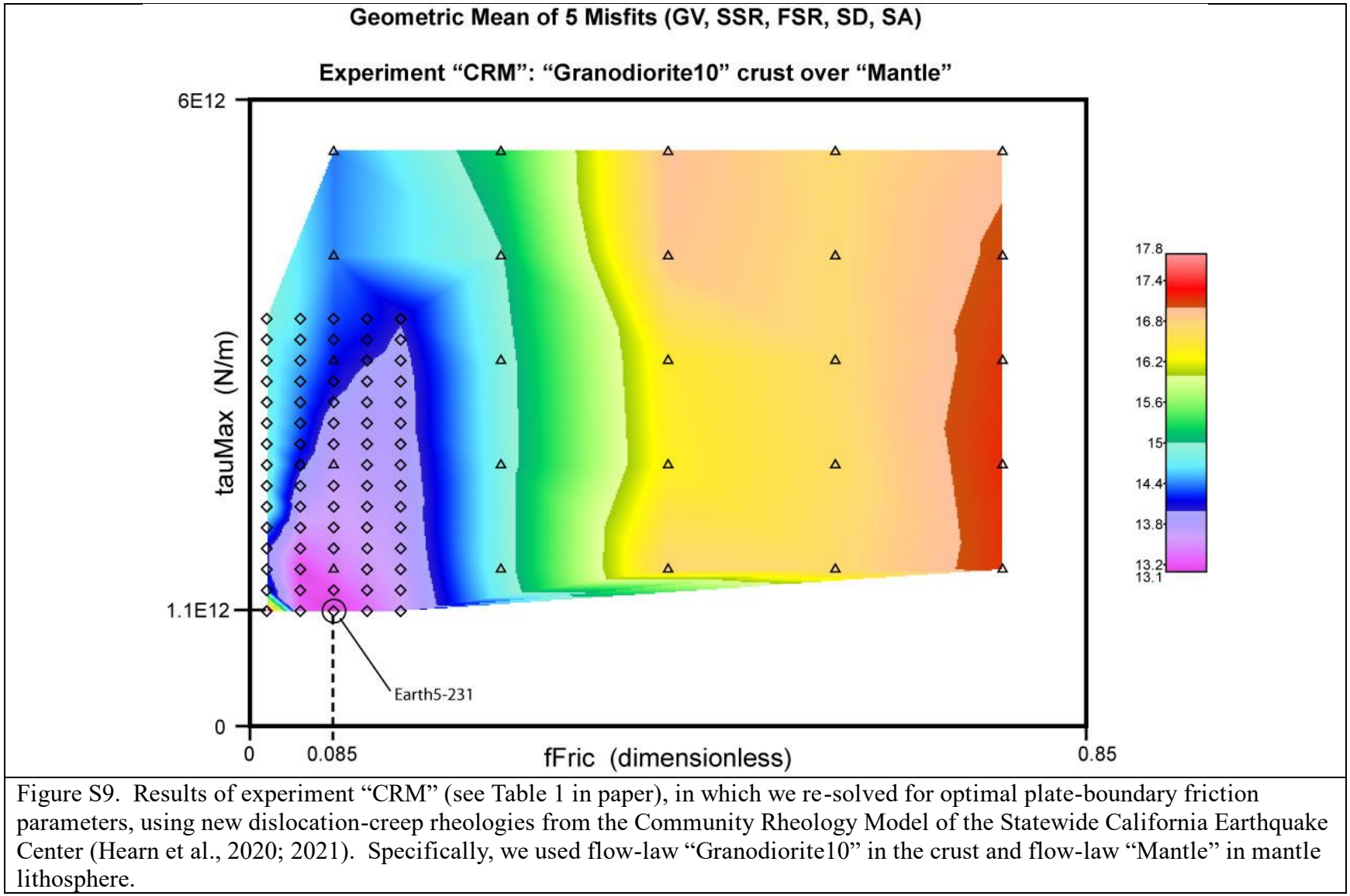

Figure S9. Results of experiment "CRM" (see Table 1 in paper), in which we re-solved for optimal plate-boundary friction parameters, using new dislocation-creep rheologies from the Community Rheology Model of the Statewide California Earthquake Center (Hearn et al., 2020; 2021). Specifically, we used flow-law "Granodiorite10" in the crust and flow-law "Mantle" in mantle lithosphere.

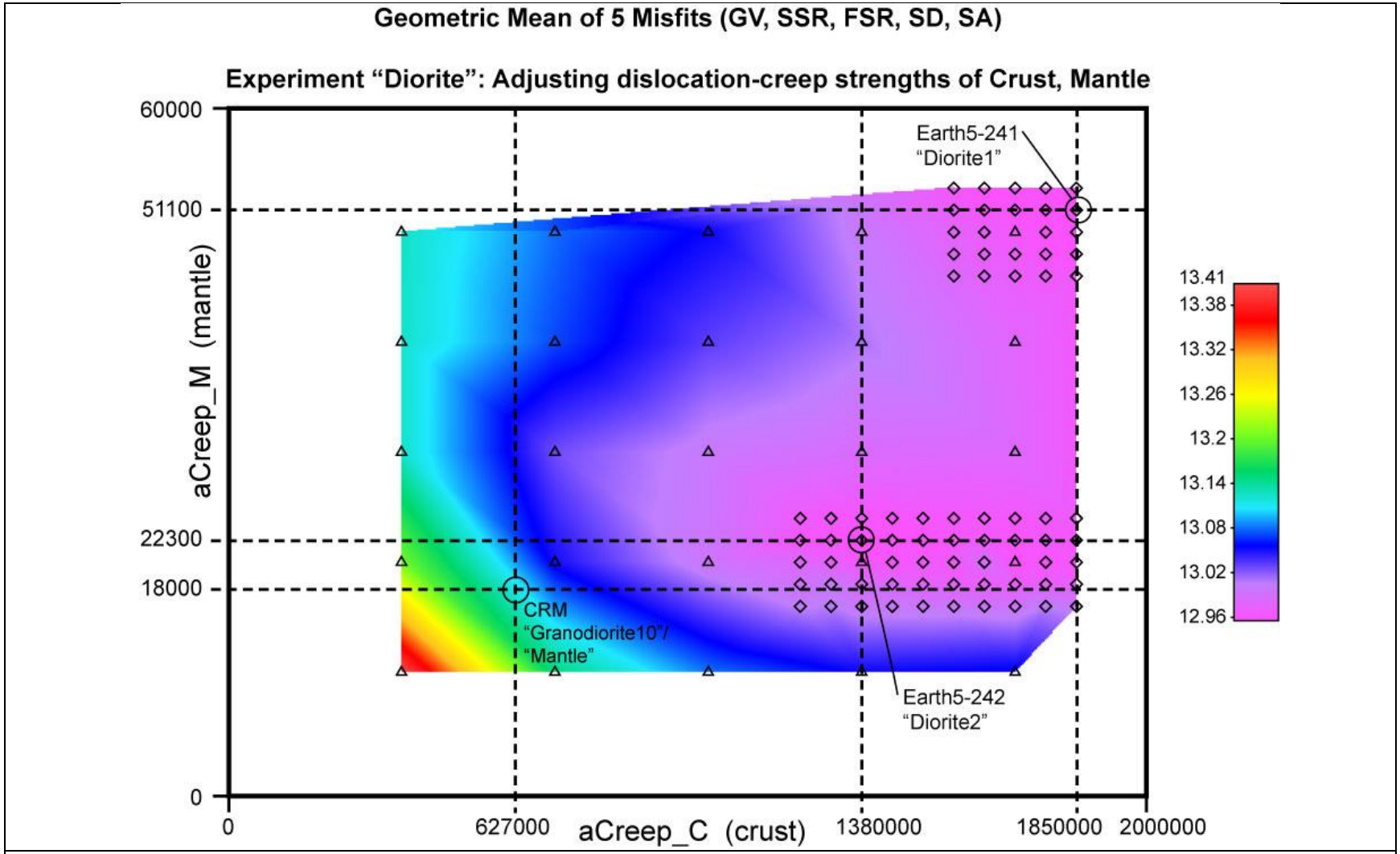

Figure S10. Results of the "Diorite" experiment (row #6 of Table 1 in main paper), in which we varied the strengths (at unit strain-rate and infinite temperature) of the dislocation creep flow-laws for both crust and mantle, starting from model "CRM". The result indicated two alternative local minima in misfit: "Diorite1" and "Diorite2". Based on our Bayesian preference for minimal changes, we prefer solution "Diorite2" in which the crustal flow-law is about twice as strong as the starting strength of "Granodiorite10".

136

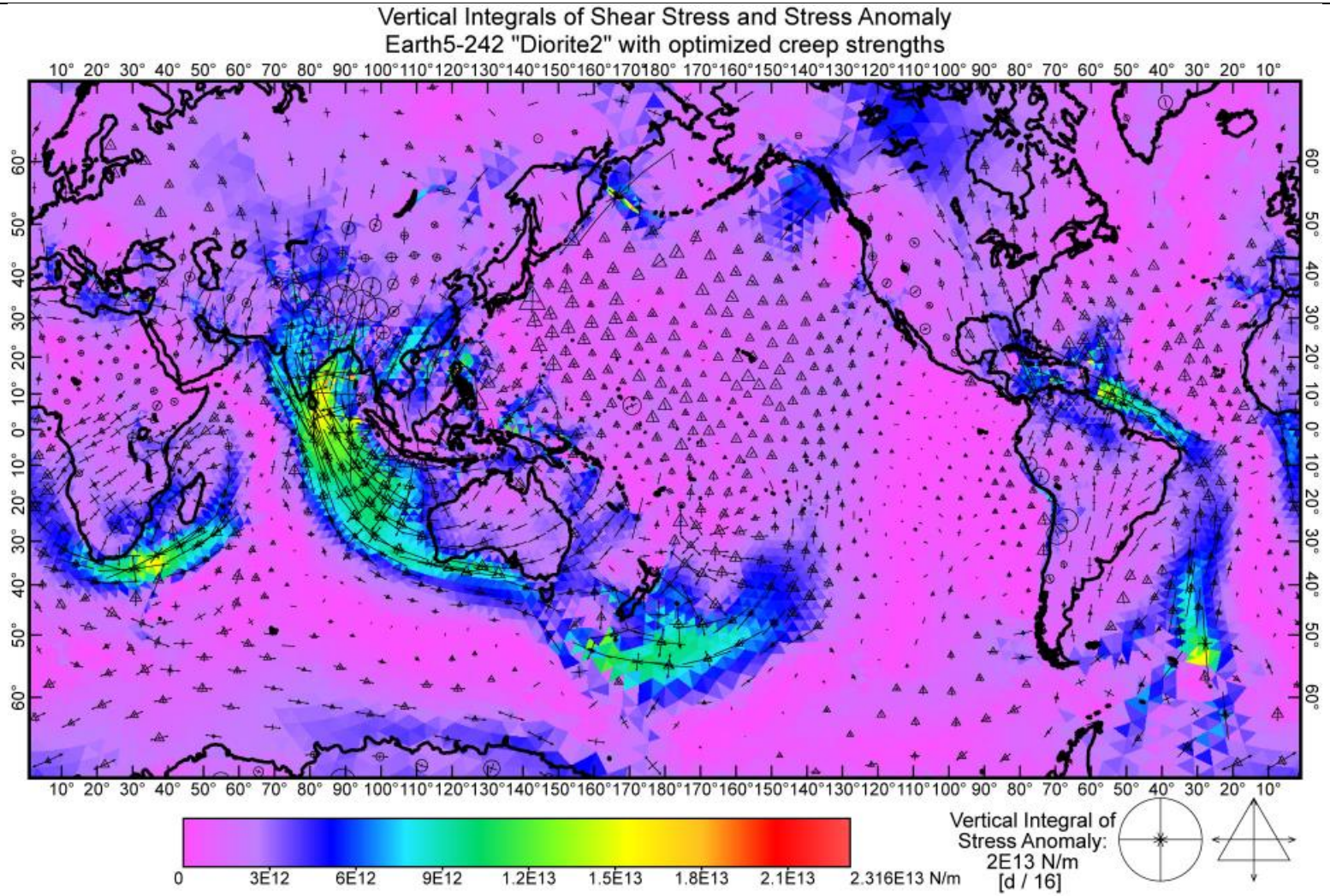

Figure S11. Vertically-integrated (through the lithosphere) values of maximum shear stress (in colors) and stress anomaly (as sample tensor symbols) in the Earth5-242 "Diorite2" model. See definition of stress anomaly in Paper I. Very high stresses are predicted in several areas where oceanic lithosphere is being deformed, but where no new plate-boundary faults have been mapped.

137

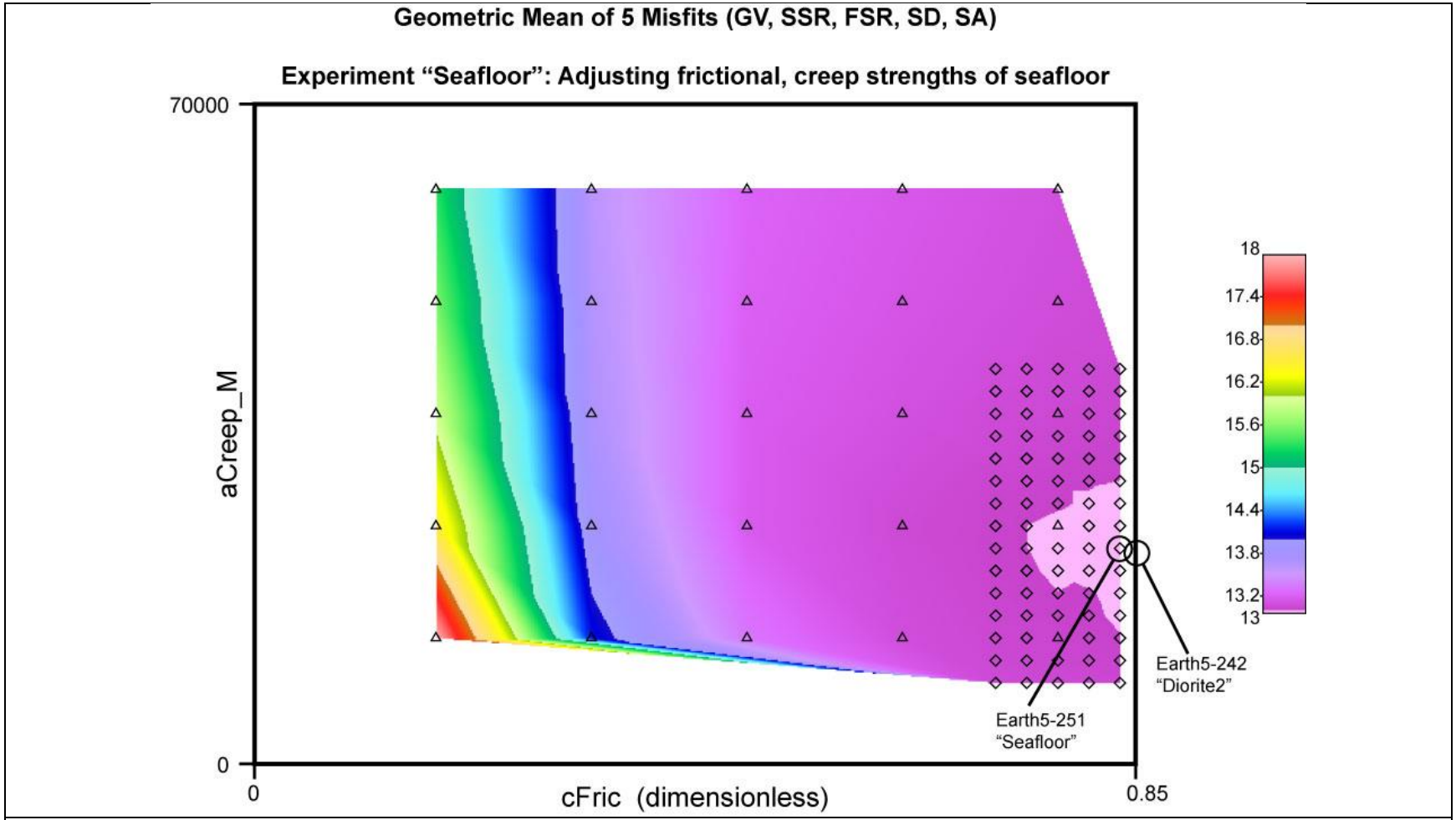

Figure S12. Results of the "Seafloor" experiment (row #7 of Table 1 in paper), in which two strength parameters were varied for oceanic lithosphere, while strength parameters for continental lithosphere were held constant. ShellSet finds that the starting parameters are optimal, and that no special weakening of oceanic lithosphere is appropriate.

138

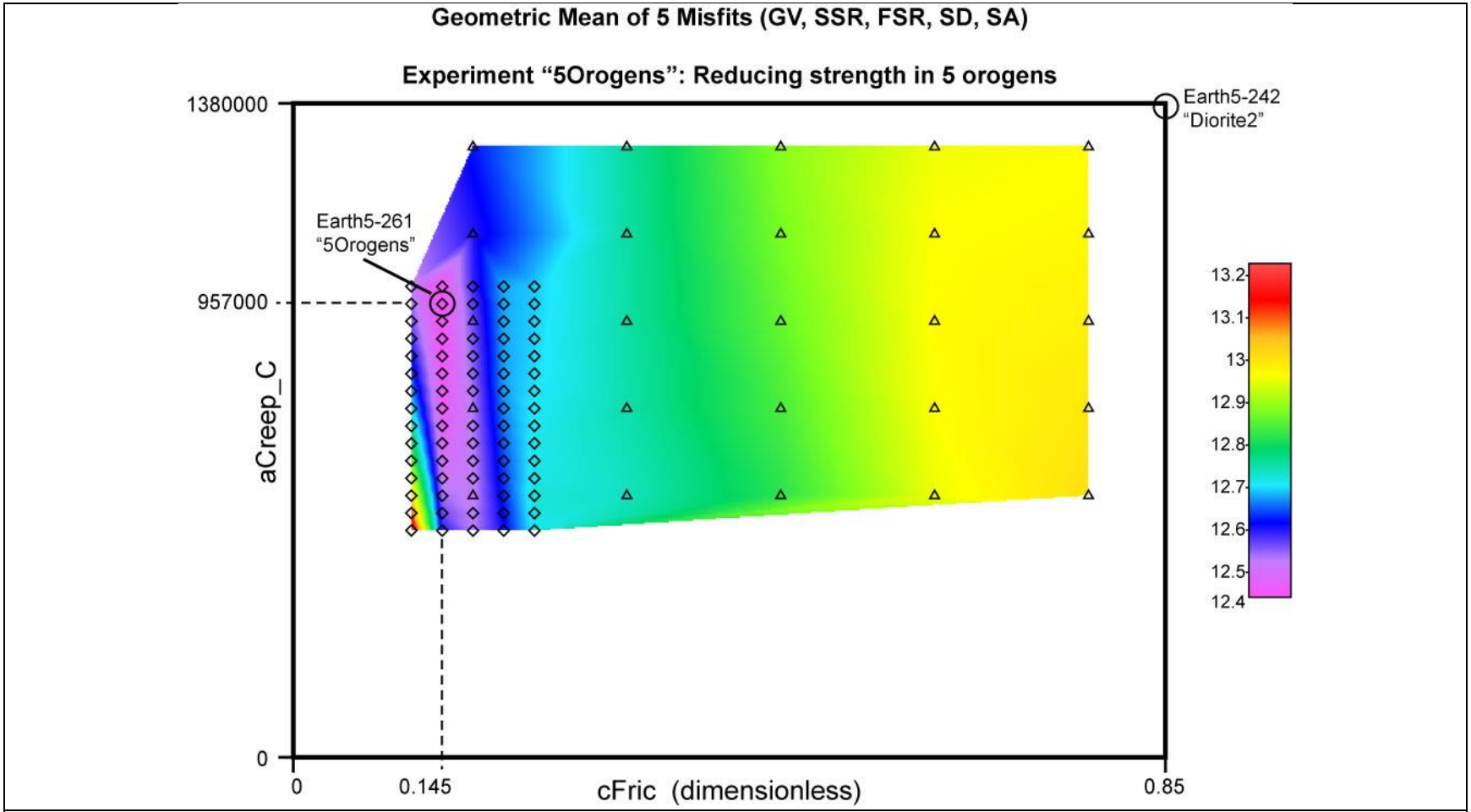

Figure S13. Results of the "5Orogens" experiment (row #8 of Table 1 in paper), in which special weakening (by reduction of continuum friction cFric and/or dislocation-creep strength aCreep_C) was attempted in 5 large orogens defined by Bird (2003), while strength parameters for all other lithosphere were held constant at "Diorite2" values. ShellSet finds that a large reduction in continuum friction would be optimal according to the geometric-mean-of-all misfits metric. However, as discussed in paper, the GV misfit went up after this adjustment, and local plots of solutions show that only the Persia-Tibet-Burma orogen benefitted from this change; the other 4 orogens developed landslides or other unphysical behaviors. Therefore, this model was not accepted as preferred.

139

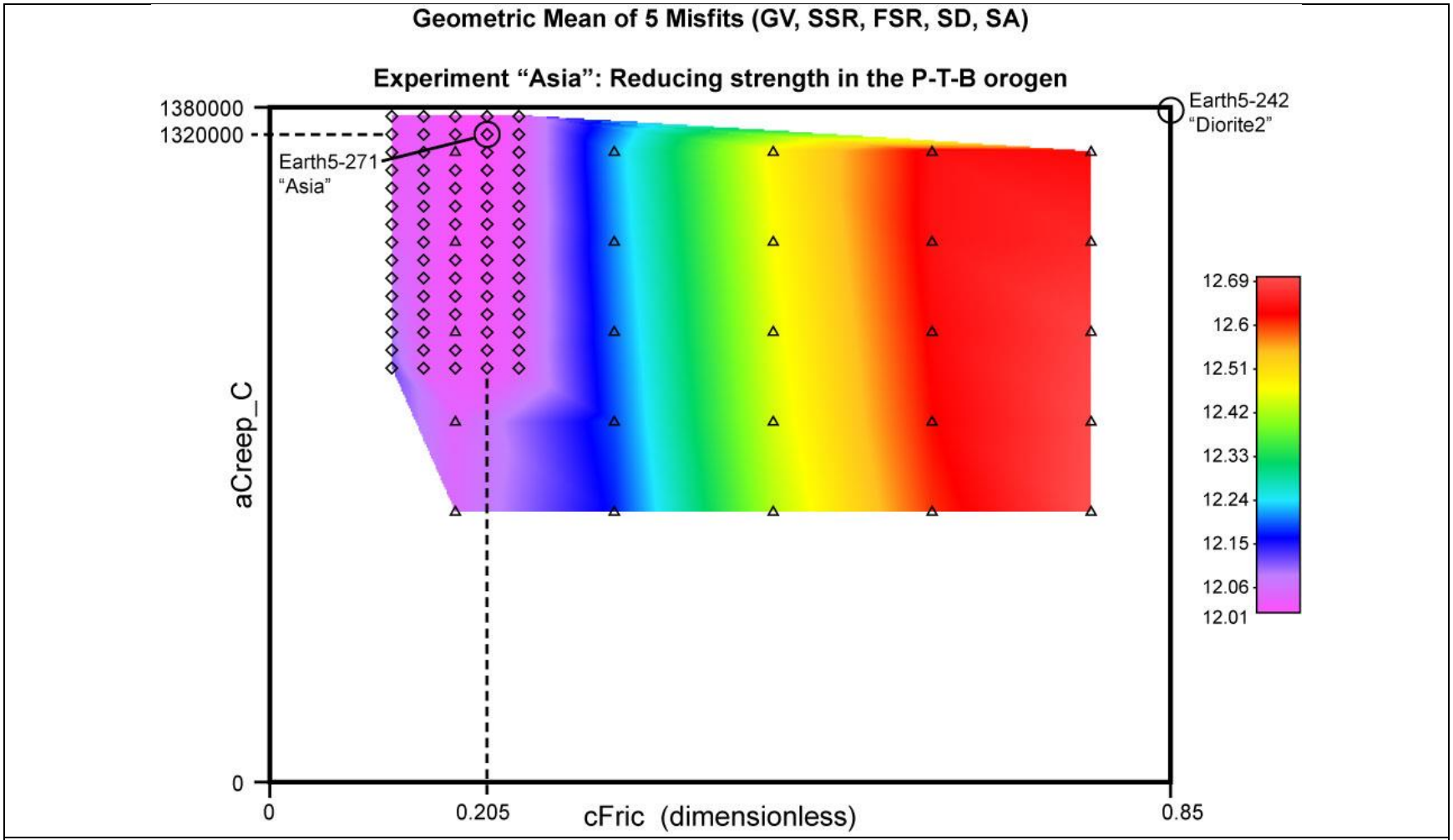

Figure S14. Results of the "Asia" experiment (row #9 of Table 1 in paper), in which only the large Persia-Tibet-Burma orogen was subject to reduced strength parameters, while strength of all other lithosphere was held constant. Because of the large reductions in mean misfit, GV misfit, SSR misfit, and SD misfit, this model Earth5-271 was adopted as our preferred model for this study. As discussed in the paper, reduced continuum friction within the PTB orogen may be a proxy for many active faults (with effective frictions near 0.085±0.034) which were possibly omitted from our model F-E grid in this complex region.

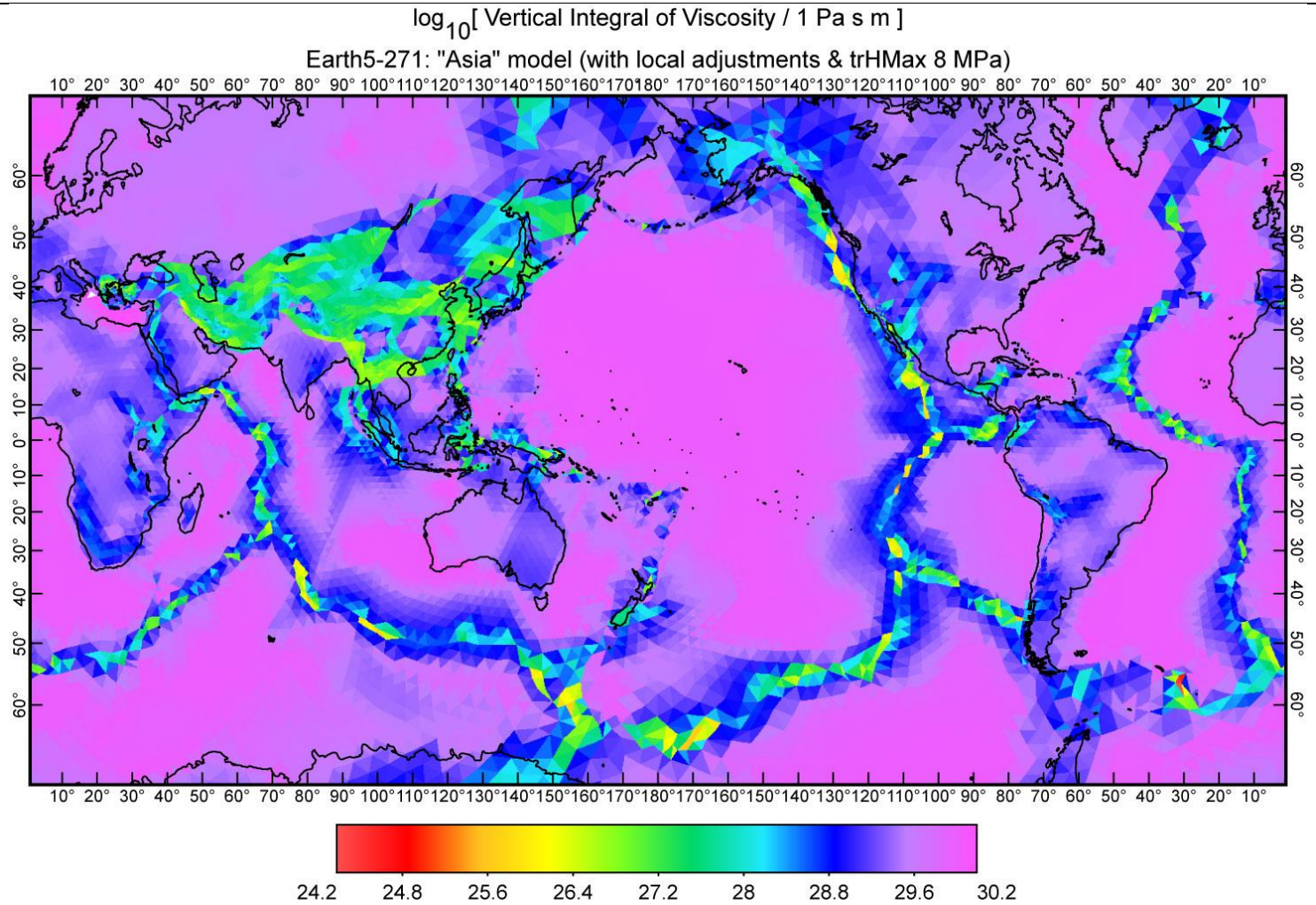

Figure S15. Vertical integrals (through the lithosphere) of effective viscosity for preferred model Earth5-271 "Asia". A logarithmic color scale is used to represent the extreme range of 6 orders of magnitude. Although ShellSet models use nonlinear flow-laws of frictional plasticity and dislocation-creep, effective viscosity can always be computed as one-half the ratio of deviatoric stress to deviatoric strain-rate at each depth-collocation point in each finite element. Those values are then vertically-integrated for this plot. In practice, effective viscosity tends to decrease with increasing strain-rate and/or heat-flow.

140

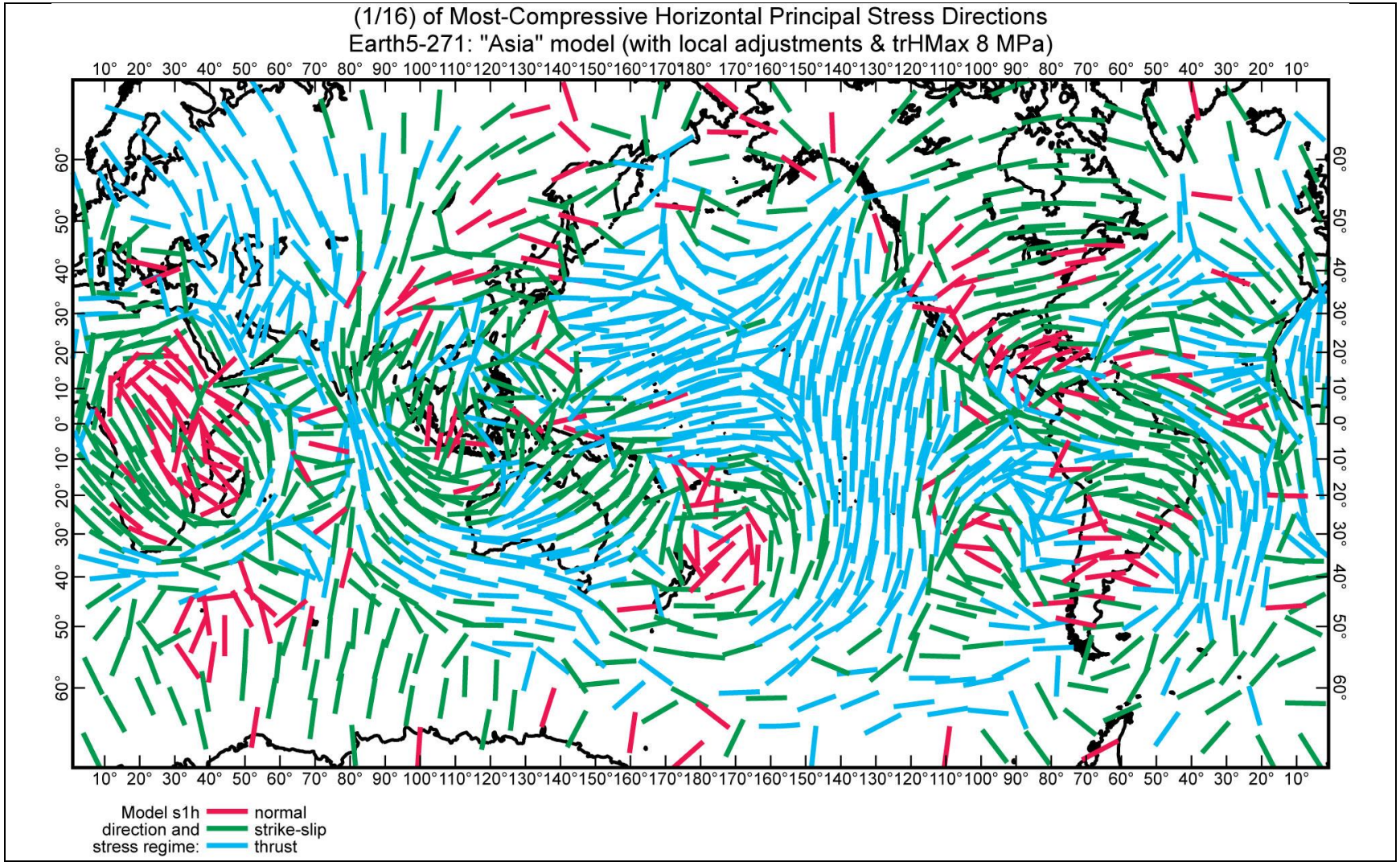

Figure S16. Azimuths of most-compressive horizontal principal stress (parallel to most-compressive horizontal principal strain-rate in isotropic continua) from preferred model Earth5-271 "Asia". Tectonic regime is indicated by symbol color. Azimuths in this figure can be compared to those of scoring dataset SD in Figure S3 above.